Single-scattering properties of triaxial ellipsoidal particles for a size parameter range from the Rayleigh to geometric-optics regimes

Lei Bi,[1] Ping Yang,[2,*] George W. Kattawar,[1] and Ralph Kahn[3]

[1]Department of Physics, Texas A&M University, College Station, Texas 77843, USA

[2]Department of Atmospheric Sciences, Texas A&M University, College Station, Texas 77843, USA

[3]Climate and Radiation Branch, NASA Goddard Space Flight Center, Greenbelt, Maryland 20771, USA

*Corresponding author: pyang@ariel.met.tamu.edu

The single-scattering properties of randomly oriented triaxial ellipsoids with size parameters from the Rayleigh to geometric-optics regimes are investigated. A combination of the discrete dipole approximation (DDA) technique and an improved geometric optics method (IGOM) is applied to the computation of ellipsoidal particle scattering properties for a complete range of size parameters. Edge effect contributions to the extinction and absorption efficiencies are included in the present IGOM simulation. It is found that the extinction efficiency, single-scattering albedo, and asymmetry factor computed from the DDA method for small size parameters smoothly transition to those computed from the IGOM for moderate-to-large size parameters. The phase matrix elements computed from these two methods are also quite similar when size parameters are larger than 30. Thus, the optical properties of ellipsoidal particles can be computed by combing the DDA and the IGOM for small-to-large size parameters. Furthermore, we also examine the applicability of the ellipsoid model to the simulation of the scattering properties of realistic aerosol particles by comparing the theoretical and experimental results for feldspar aerosols. It is shown that the ellipsoid model is better than the commonly used spheroid model for simulating dust particle optical properties, particularly, their polarization characteristics, realistically.   © 2008 Optical Society of America

OCIS codes: 290.0290, 080.0080, 260.0260, 010.0010.

1. Introduction

The nonsphericity of airborne dustlike particles has been widely recognized as an important factor in remote sensing of the optical and microphysical properties of these particles. Especially, it has been shown that neglecting the nonsphericity of aerosol particles may lead to large errors in aerosol property retrieval [1–4]. The scanning electron microscope (SEM) images of some sampled aerosol particles [5] show that the morphologies of these irregular particles are very complicated. Specifically, these particles have small-scale structures but lack well-defined overall shapes. In numerical modeling of the optical properties of dust particles, it is unrealistic to account for the morphological details of these particles. The application of simple geometries to complex particle optical property simulation has been discussed by Macke and Mishchenko [6] and Kahnert *et al.* [7]. To account for the nonsphericity in many previous studies reported in the literature, rounded dust particles (for example, Saharan dust) are usually assumed to be spheroids (i.e., ellipsoids of revolution) as a first-order approximation for the overall shapes of these particles [8–11], although some more complicated particle geometries have also been considered (e.g., [12,13]). Realistic dust aerosols are almost

exclusively irregular particles without any particular symmetry. It is shown that retrieving mineral aerosol particle complex refractive index based on the spheroidal model from measured scattering matrices [5] always overestimates the imaginary part. To match theoretical simulations with measurements, one has to use nonphysical complex refractive indices and shape distributions [14].

It requires one degree of freedom (i.e., particle size) to specify the geometry of a spherical particle, whereas two degrees of freedom (the particle maximum dimension and aspect ratio) are needed to specify the geometry of a spheroidal particle. The dimensions of an ellipsoid along three orthogonal axes may be different. Thus, ellipsoid geometry has one more degree of freedom than the commonly-used spheroid geometry, and the former is a better approximation to the shapes of realistic dust particles. Ghobrial and Sharief [15] estimated that the aspect ratios of the three axes (hereafter, indicated by a, b, and c) of sandstorm particles are approximately $c:b = 1:0.71$ and $b:a = 0.71:0.53$. For simplicity, in the following discussions the two aspect ratios, $c:b = 1:0.71$ and $b:a = 0.71:0.53$, are indicated in a concise form given by $c:b:a = 1:0.71:0.53$.

In this paper we investigate the single-scattering properties of dielectric and homogeneous ellipsoidal particles for a complete size parameter spectrum. The analytical solution to the scattering of light by an ellipsoid has been partially solved [16–18]. However, the analytical solution is computationally stable only in the case of quite small particles. To compute the single-scattering properties of ellipsoids with size parameters required for practical remote sensing applications, numerical methods, such as the T-matrix [19–21], discrete dipole approximation (DDA) [22,23], finite-difference time domain (FDTD) [24,25], and pseudospectral time domain (PSTD) methods [26,27] can be used for small to moderate size parameters. For large particles, approximate approaches such as the anomalous diffraction theory [28] and the so-called physical optics approximation method [29] have been applied to arbitrarily oriented ellipsoids. However, in both the approximate methods, only the angular patterns of the scattered light associated with oriented ellipsoids have been studied. For many practical applications involved in atmospheric radiative transfer simulation and remote sensing, it is necessary to compute the full scattering matrix, extinction efficiency, and single-scattering albedo of randomly oriented particles. In this study, we employ the improved geometric optics method (IGOM) developed by Yang and Liou [30], and a DDA code (ADDA 0.77) developed by Yurkin and Hoekstra [23] to compute a complete set of optical properties for large and small ellipsoidal particles, respectively.

In the computation of the extinction and absorption efficiencies, the IGOM, which only considers reflection, refraction, and diffraction, underestimates the values of the aforementioned optical quantities because the edge effect is neglected. The edge effect contribution to the extinction efficiency has been extensively discussed in the cases of spheres, spheroids, and cylinders [31–35]. Baran and Havemann [36] and Mitchell et al. [37] studied the edge effect contributions to the absorption and extinction efficiencies of hexagonal ice crystals, respectively. Furthermore, Mitchell et al. [38] have incorporated the edge effects (or, photon tunneling, a term used in their study) into a modified anomalous diffraction approximation to compute the absorption and extinction coefficients of water and ice clouds. Because it is quite difficult to obtain an analytical expression for the edge effect contribution in the case of ellipsoids, in this paper we develop an efficient numerical method to compute the edge effect contribution for the scattering of light by randomly oriented ellipsoids. For the absorption efficiency, we develop a semiempirical method to incorporate so-called above- and below-edge contributions, following Nussenzveig and Wiscombe [39–41], who applied the complex angular momentum (CAM) theory to the scattering of light by spheres (or spherical well potentials in quantum physics).

This paper is organized as follows: Section 2 is a brief introduction to the DDA method. Section 3 presents the theory of the IGOM, which contains the description of geometry, the ray-tracing technique, and the treatment of diffraction. The edge effect contributions to the extinction and absorption efficiencies are discussed in Section 4. In Section 5, we present the single-scattering properties of ellipsoids and compare the theoretical simulations and measurements of the phase matrices for feldspar aerosol particles. Finally, the conclusions of this study are given in Section 6.

2. DDA Method

DDA is one of several popular numerical methods for computing the scattering properties of an arbitrarily shaped particle with a small/moderate size parameter [42]. In DDA, an irregular particle is discretized into an array of small volumes. Each small volume is approximated as an electric dipole [43]. When an electromagnetic wave is incident on the particle, each dipole oscillates in response to the incident field and the induced field associated with all other dipoles. Mathematically, the basic DDA equation is in the form of

$$\vec{E}_i^{\text{inc}} = \alpha_i^{-1}\vec{P}_i - \sum_{j \neq i} G_{ij}\vec{P}_j, \tag{1}$$

where $\vec{E}_i^{\text{inc}}$ is the incident electric field, $\vec{P}_i$ is the polarizaton of each dipole, α_i is the polarizability, and G_{ij} is the discretized Green's function. When a self-consistent solution to the DDA equation is obtained, it is straightforward to calculate the scattering properties of the particle on the basis of a volume-integral electromagnetic relation that maps the near-field to

the far-field [44]. The formulation of the DDA equation as derived from the basic volume integral equation can also be found in [45]. Various numerical aspects of this method, such as iterative methods and convergence analysis, have been recently reviewed by Yurkin and Hoekstra [46]. Note that the DDA method has been extensively employed by other researchers (e.g., [13,47]) to investigate the optical properties of dust particles.

3. IGOM

The IGOM is a hybrid algorithm based on the principles of geometric optics and electromagnetic wave theory [30]. Specifically, this method employs the ray-tracing technique to compute the near-field on the scattering particle surface. The corresponding far-field is obtained by mapping the near-field to its counterpart in the radiation zone on the basis of electromagetic wave theory. The basic formulation of the IGOM can be found in Yang and Liou [30]. To increase the computational efficiency of the IGOM, the Monte Carlo method [48] is applied to the ray-tracing technique and a simplified algorithm is used to account for the ray-spreading effect associated with mapping the near-field to the far-field.

A. Geometry

Figure 1 shows the geometry of an ellipsoid and the configurations of two coordinate systems. The geometry of an ellipsoid centered at the origin can be completely described by its surface equation in the Cartesian coordinate system $oxyz$ as follows:

$$\frac{x^2}{a^2} + \frac{y^2}{b^2} + \frac{z^2}{c^2} = 1, \tag{2}$$

where a, b, and c are principal radii (or semi axes) along three orthogonal directions. When any two of them, say a and b, are the same, the ellipsoid reduces to a spheroid. The $oxyz$ coordinate system is usually called the particle coordinate system, distinguished from the incident ray coordinate system $ox'y'z'$ used
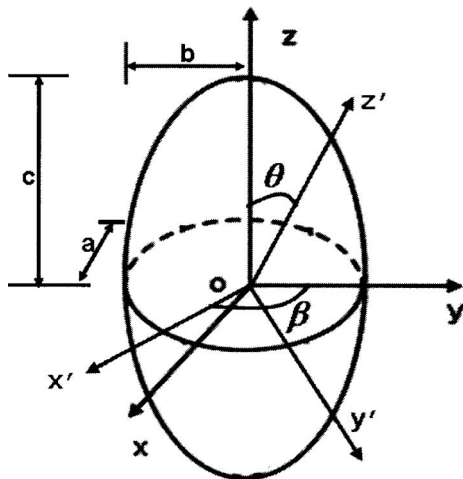

Fig. 1.   Geometry of a non-axially-symmetric ellipsoid in $oxyz$ and $ox'y'z'$ coordinate systems.

for specifying the scattering angle and the scattering plane. In this study, the direction of the incident ray is along oz', and the directions of parallel and perpendicular polarizations are specified along the x' and y' axes, respectively. The coordinate transformation from $ox'y'z'$ to $oxyz$ is given by

$$\begin{pmatrix} x \\ y \\ z \end{pmatrix} = \begin{pmatrix} \sin\beta & -\cos\beta & 0 \\ \cos\beta & \sin\beta & 0 \\ 0 & 0 & 1 \end{pmatrix} \begin{pmatrix} 1 & 0 & 0 \\ 0 & \cos\theta & \sin\theta \\ 0 & -\sin\theta & \cos\theta \end{pmatrix}$$

$$\begin{pmatrix} x' \\ y' \\ z' \end{pmatrix} = \begin{pmatrix} \sin\beta & -\cos\theta\cos\beta & -\sin\theta\cos\beta \\ \cos\beta & \cos\theta\sin\beta & \sin\theta\sin\beta \\ 0 & -\sin\theta & \cos\theta \end{pmatrix} \begin{pmatrix} x' \\ y' \\ z' \end{pmatrix}, \tag{3}$$

where θ and β are two angles that specify the direction of the incident ray in the particle coordinate system. In the incident ray coordinate system, the surface equation of the ellipsoid is given by

$$Dz' = -E \pm abc\sqrt{D - (Ax'^2 + By'^2 + Cx'y')}, \tag{4}$$

where

$$A = (a^2 - b^2)\cos^2\theta\cos^2\beta + b^2\cos^2\theta + c^2\sin^2\theta,$$

$$B = a^2\sin^2\beta + b^2\cos^2\beta,$$

$$C = (a^2 - b^2)\sin(2\beta)\cos\theta,$$

$$D = c^2\sin^2\theta(a^2\sin^2\beta + b^2\cos^2\beta) + a^2b^2\cos^2\theta,$$

$$E = (a^2 - b^2)c^2\sin\beta\cos\beta\sin\theta x'$$
$$\quad + [a^2(c^2 - b^2) + c^2(b^2 - a^2)\cos^2\beta]\sin\theta\cos\theta y'.$$

The plus and minus signs in Eq. (4) describe the illuminated and nonilluminated sides, respectively. The edge (or shadow boundary) that connects the illuminated and nonilluminated sides is determined by the following equation:

$$Ax'^2 + By'^2 + Cx'y' = D; \qquad z' = -E/D. \tag{5}$$

It can be shown that the interface of the illuminated and nonilluminated sides is an ellipse, and its semi axes are

$$\bar{a} = \sqrt{\frac{D(1 - \tan^2\omega)}{A - B\tan^2\omega}}, \tag{6}$$

$$\bar{b} = \sqrt{\frac{D(1 - \tan^2\omega)}{B - A\tan^2\omega}}, \tag{7}$$

where ω is given by

$$\omega = \frac{1}{2}\arctan\frac{C}{B-A}. \qquad (8)$$

Note that the plane containing the ellipse is not perpendicular to the direction of the incident light, and ω is zero for spheroids, i.e., when a is equal to b. It can be proved that the projected area is

$$S = \pi\bar{a}\bar{b} = \pi\sqrt{D}. \qquad (9)$$

Employing the following transformation:

$$x' = \cos\omega\bar{x}' + \sin\omega\bar{y}', \qquad (10)$$

$$y' = -\sin\omega\bar{x}' + \cos\omega\bar{y}', \qquad (11)$$

which means the rotation from $o - x'y'$ to $o - \bar{x}\bar{y}$ by an angle ω, we obtain a similar ellipse equation for the projection of the particle onto the $ox'y'$ plane, given by

$$\frac{\bar{x}'^2}{\bar{a}^2} + \frac{\bar{y}'^2}{\bar{b}^2} = 1. \qquad (12)$$

The preceding ellipsoid geometry description in both the particle coordinate system and the incident coordinate system is quite useful in the ray-tracing, diffraction, and edge effect calculations. Similar results can be found in [28], where the differences in formula are due to different coordinate conventions and definitions of the Euler angles.

B. Ray Tracing

The basic principle of the IGOM is to calculate the electromagnetic field on the surface of the ellipsoid by using the ray-tracing technique, as illustrated in Fig. 2. The corresponding far-field is obtained by mapping the near-field to its counterpart in the radiation (or, far-field) zone. The magnitude and phase of each ray is calculated based on the localized-plane-wave approximation by using the Fresnel formulas. The directions of external reflection, internal reflection, and refraction are determined by Snell's law. The first step for the ray-tracing calculation is to initialize the incident rays and determine the intersection points. The intersection points of the incident rays with the particle are determined by the Monte Carlo method in the incident coordinate system as follows:

$$x' = \bar{a}\sqrt{\xi}\cos\omega\cos(2\pi\chi) + \bar{b}\sqrt{\xi}\sin\omega\sin(2\pi\chi), \quad (13)$$

$$y' = -\bar{a}\sqrt{\xi}\sin\omega\cos(2\pi\chi) + \bar{b}\sqrt{\xi}\cos\omega\sin(2\pi\chi), \quad (14)$$

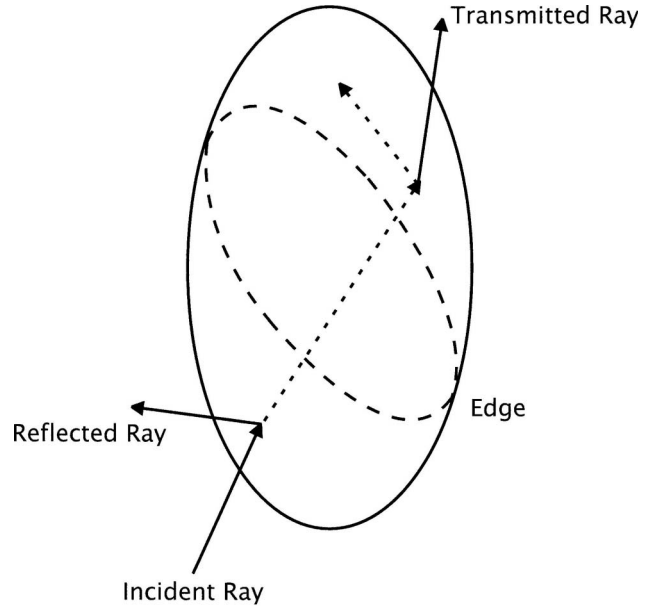$$z' = [-E - abc\sqrt{D - (Ax'^2 + By'^2 + Cx'y')}]/D, \quad (15)$$

Fig. 2. Schematic geometry for the ray-tracing calculations involving a triaxial ellipsoid.

where ξ and χ are two random numbers with a uniform probability distribution between 0 and 1. The ray-tracing process is carried out in the particle system, in which the incident point coordinates are obtained by the coordinate transformation given by Eq. (3). According to Snell's law, the surface normal direction $\hat{n}$ at the incident point (x_1, y_1, z_1) is needed to determine the reflection and refraction directions. Given the surface Eq. (2), we have

$$\hat{n} = (x_1/a^2, y_1/b^2, z_1/c^2)/\sqrt{x_1^2/a^4 + y_1^2/b^4 + z_1^2/c^4}. \qquad (16)$$

Given the initial point (x_1, y_1, z_1) on the surface and direction of the ray within the particle, the ray-tracing process requires the next intersection point (x_2, y_2, z_2), which can be determined by

$$(x_2, y_2, z_2) = (x_1, y_1, z_1) + d(v_1, v_2, v_3), \qquad (17)$$

$$d = -\frac{2x_1v_1/a^2 + 2y_1v_2/b^2 + 2z_1v_3/c^2}{v_1^2/a^2 + v_2^2/b^2 + v_3^2/c^2}, \qquad (18)$$

where d is the length of the internal ray and (v_1, v_2, v_3) is the unit vector of its direction. Using Eqs. [16–18], Snell's law, and the Fresnel formulas, the ray-tracing calculation can be carried out until the energy associated with the ray of interest is effectively negligible (say, 10^{-5}). The technical details associated with the electromagnetic field computation in the ray-tracing technique can be found in Yang and Liou [30].

C. Diffraction

In addition to the contributions from the reflected and refracted rays involved in the ray-tracing calculation, the diffraction of the incident wave also contributes to the scattered energy. Using the surface mapping technique, Yang and Liou [30] showed that the amplitude scattering matrix for diffraction is given as follows:

$$A_{\text{dif}} = \frac{k^2}{2\pi} I_s \begin{bmatrix} (\cos\theta_s + \cos^2\theta_s)/2 & 0 \\ 0 & (1+\cos\theta_s)/2 \end{bmatrix},$$

(19)

$$I_s = \int\int_s \exp(-ik\hat{r}\cdot\vec{\xi})\mathrm{d}^2\xi,$$

(20)

where θ_s is the scattering angle, s is the projected area, k is the wave number, and $\hat{r}$ is a unit vector pointing along the observational direction, as illustrated in Fig. 3. The explicit form of the integral in Eq. (20) for an ellipse can be given in the form of

$$I_s = \pi\bar{a}\bar{b}\frac{2J_1(k\sin\theta_s\sqrt{\bar{a}^2\cos^2\phi + \bar{b}^2\sin^2\phi})}{k\sin\theta_s\sqrt{\bar{a}^2\cos^2\phi + \bar{b}^2\sin^2\phi}}, \quad (21)$$

where J_1 is the first-order Bessel function, and ϕ is the azimuthal angle, which specifies the scattering plane.

4. Edge Effect

When a plane wave is incident on a scattering particle with a smooth surface whose radius of curvature is much larger than the incident wavelength, the transition or penumbra region between illuminated
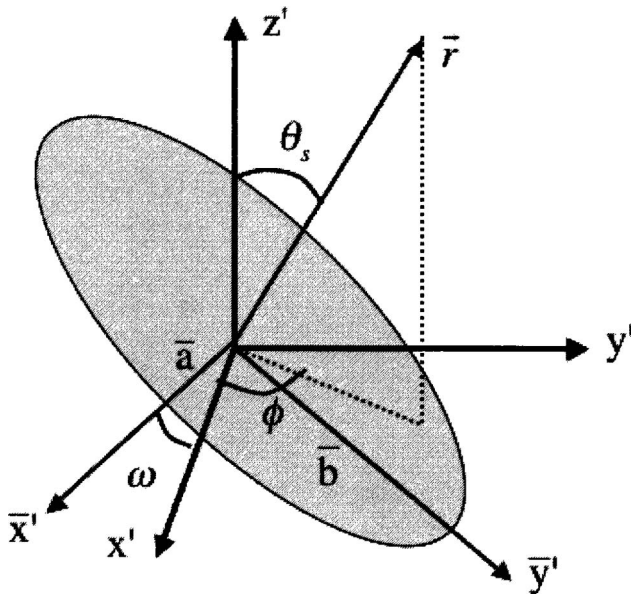

Fig. 3. Diffraction of an ellipsoid with an elliptic projection. Semi axes $\bar{a}$ and $\bar{b}$ and rotation angle ω are defined in Eqs. (6)–(8).

and nonilluminated sides of the particle leads to an additional term. This term is known as the edge effect contribution to the scattering amplitude matrix in the forward direction, which also contributes to the extinction efficiency[35]. In principle, the IGOM considers only the reflection, refraction, and diffraction of the incident light and neglects the nonzero edge effect contribution. Note that by including the edge effect contribution in the geometric optics method, the extinction efficiency will converge to 2 asymptotically from above [33,35].

To quantitatively include the edge effect, Jones [32] assumed that the neighborhood of a point on the edge behaves locally like that associated with a cylinder, and the edge effect contribution to the extinction efficiency of a convex particle for one certain orientation can be given as follows:

$$Q_{e,\text{edge}} = \frac{c_0}{k^{2/3}S}\int R(s)^{1/3}\sin^{1/3}\alpha(s)\mathrm{d}s,$$

(22)

where c_0 is a universal constant, R is the radius of curvature of the "profile" of the edge, S is the projected area, α is the angle between the incident direction and the tangent of the edge, and $\mathrm{d}s$ is the arc length of the edge. In Jones' treatment, the particle is perfectly conducting. The extinction efficiency derived from Eq. (22) in the case of a sphere is

$$Q_{e,\text{edge}} = \frac{2c_0}{(kR)^{2/3}},$$

(23)

$$2c_0 = c_{\text{TM}} + c_{\text{TE}} = 0.1322,$$

(24)

where k is the wavenumber and R is the radius, and c_{TM} and c_{TE} are two coefficients corresponding to the TM and TE waves. Jones' result [32] is exactly the same as the first correction to the geometric-optics result obtained by Rubinow and Wu [49] from Mie theory. For a transparent sphere, Nussenzveig and Wiscombe [39] find that the first term due to the edge effect has the same form as Eq. (23), but with $c_0 = 0.996193$. Following Jones' approach but with c_0 replaced by 0.996193, Fournier and Evans [33] explicitly derived a general formula for $Q_{e,\text{edge}}$ for the case of spheroids. For spheroids, it can be shown that $\alpha = 0$, i.e., the incident direction is always perpendicular to the plane coinciding with the edge plane. For triaxial ellipsoids, α is a function of the position on the edge. It is difficult to obtain an analytical formula for the edge effect in the case of triaxial ellipsoids because of the inherent mathematical complexity. However, we develop a numerical method to compute it accurately, which is described in Appendix A. For random orientations, the average of the edge effect contribution to the extinction efficiency is given by

$$\langle Q_{e,\text{edge}}\rangle = \frac{\int_0^1\int_0^{\pi/2} Q_{e,\text{edge}}D^{1/2}\mathrm{d}\mu\mathrm{d}\beta}{\int_0^1\int_0^{\pi/2} D^{1/2}\mathrm{d}\mu\mathrm{d}\beta},$$

(25)

where $\mu = \cos\theta$; θ and β are the same angles as used in Fig. 1. Because geometrical rays and the edge effect contribute independently to the amplitude scattering matrix in the forward direction, the total extinction efficiency is given by the sum of the IGOM result and $\langle Q_{e,\text{edge}} \rangle$ as follows:

$$\langle Q_e \rangle = \langle Q_{e,\text{IGOM}} \rangle + \langle Q_{e,\text{edge}} \rangle, \tag{26}$$

where $Q_{e,\text{IGOM}}$ is calculated by the IGOM.

The edge effect contribution to the extinction efficiency can also be understood as an additional "blocking" effect. In the framework of the interaction between photons and a sphere, those photons with impact parameters larger than the radius of the sphere are able to penetrate the boundary. This process is known as the above edge effect or "tunnelling" effect, which is in principle a wave phenomenon. When photons hit on the sphere within a fraction $(kR)^{-2/3}$ of the full radius from the edge, a particular interference (anomalous reflection due to centrifugal barrier) occurs [35]. This phenomenon is called the below-edge effect. This anomalous neighborhood where the edge effect plays a role is termed an "edge strip", and has been estimated [41] (WKB approximation) as follows:

$$R_0 \le r \le R_0 \left[1 + c_+ \left(\frac{2}{kR_0} \right)^{2/3} \right] \quad \text{(above edge)}, \tag{27}$$

$$R_0 \left[1 - c_- \left(\frac{2}{kR_0} \right)^{2/3} \right] \le r \le R_0 \quad \text{(below edge)}, \tag{28}$$

where R_0 is the radius of sphere, and c_+ and c_- are positive numerical constants of order unity. It is straightforward to calculate the additional extinction efficiency due to the edge effect. Specifically, after the higher order term is omitted, the edge contribution is $2^{2/3}(c_+ + c_-)2/(kR_0)^{2/3}$, similar to Eq. (23).

Both the above-edge and below-edge effects contribute to the absorption efficiency. Nussenzveig and Wiscombe [39] showed that

$$Q_a = Q_{a,\text{GOM}} + Q_{a,a.e.} + Q_{a,b.e.}, \tag{29}$$

where $Q_{a,a.e.}$ and $Q_{a,b.e.}$ are the so-called above-edge and below-edge terms [39,40]. For nonspherical and randomly oriented ellipsoids, the IGOM also underestimates the absorption efficiency. The reason is that the above-edge and below-edge contributions are neglected. Note that the below-edge contribution is smaller than the above-edge effect. To incorporate the above- and below-edge effects, we develop a semi-empirical method. In this method, for each orientation of the ellipsoid, we expect the edge effect of the ellipsoid is more or less the same as that of a sphere, provided that they have the same "edge strip" area. For a sphere, the "edge strip" area can be computed as follows:

$$A_{\text{sph}} = 2(c_+ + c_-)\pi R_0^{4/3} \left(\frac{2}{k} \right)^{2/3}. \tag{30}$$

For a general ellipsoid, the effective "edge strip" area is

$$A_{\text{ell}} = (c_+ + c_-) \int R^{1/3} \left(\frac{2}{k} \right)^{2/3} ds, \tag{31}$$

where R is the radius of curvature of the profile of the edge. Therefore, a sphere has the same "edge strip" area as that of the ellipsoid for a certain orientation, if the radius of the sphere is given by

$$R_0 = \left[\frac{\int R^{1/3} ds}{2\pi} \right]^{3/4}. \tag{32}$$

The volume of the particle is another factor that influences the value of the absorption efficiency. If a sphere of radius R_0 is used for calculating the edge effect contribution, the volume of the sphere should be different from that of an ellipsoid. Therefore, we introduce a correction factor as follows:

$$f_c = \frac{1 - \exp(-km_i r_e)}{1 - \exp(-km_i R_0)}, \tag{33}$$

where r_e is the effective radius and m_i is the imaginary part of the refractive index. For an ellipsoid, r_e is given as follows:

$$r_e = \frac{2abc}{a^2 + ba^2/\sqrt{c^2 - a^2}F(\Omega, q) + b\sqrt{c^2 - a^2}E(\Omega, q)}, \tag{34}$$

where

$$q = \frac{c}{b} \sqrt{\frac{b^2 - a^2}{c^2 - a^2}}, \qquad \Omega = \arcsin\left[\sqrt{1 - a^2/c^2} \right]. \tag{35}$$

In Eq. (34), $F[\Omega, q]$ and $E[\Omega, q]$ are incomplete elliptical functions [50], given by

$$\begin{aligned} F[\Omega, q] &= \int_0^\Omega \frac{dt}{\sqrt{1 - q^2 \sin^2 t}}, \\ E[\Omega, q] &= \int_0^\Omega \sqrt{1 - q^2 \sin^2 t}\, dt. \end{aligned} \tag{36}$$

It is evident from the preceding discussions that the absorption efficiency with corrected terms can be expressed as follows:

$$Q_a(a,b,c,k,m) = Q_{a,\text{IGOM}}(a,b,c,k,m) + \frac{\int_0^1 \int_0^{\pi/2} (Q_{a,a.e.}[R_0(\mu,\beta),k,m] + Q_{a,b.e.}[R_0(\mu,\beta),k,m])f_c R_0^2 \mathrm{d}\mu \mathrm{d}\beta}{\int_0^1 \int_0^{\pi/2} D^{1/2} \mathrm{d}\mu \mathrm{d}\beta}. \quad (37)$$

It should be pointed out that we assumed $a < b < c$ in Eq. (34); otherwise, we need to reorder a, b, and c so that the Eq. (34) is correctly used. In this study we use the computer code developed by Nussenzveig and Wiscombe [39] to compute $Q_{a,a.e.}(R_0,k,m)$ and $Q_{a,b.e.}(R_0,k,m)$.

5. Results and Discussions

A. Integrated Scattering Properties

Figure 4(a) shows the extinction efficiency, absorption efficiency, single-scattering albedo, and asymmetry factor of randomly oriented ellipsoids at $0.66\,\mu$m wavelength. The refractive index is $1.53 + i0.008$ based on Levoni *et al.* [51]. The axis ratios are assumed to be $a\!:\!b\!:\!c = 0.53\!:\!0.71\!:\!1$. The size parameter is defined in terms of the radius of equivalent volume spheres. The ADDA code is employed for size parameters ranging from 0.5 to 30. The IGOM code with the inclusion of the edge effect is applied to a size parameter region from 15 to 1000. Agreement is shown for size parameters between 15 and 30, which means that the IGOM is successfully extended to the small size parameter region (~15) by

adding the missing physics (i.e., the edge effect contributions). Additionally, the absorption efficiency for size parameters from the Rayleigh to geometric-optics regimes can also be effectively computed in the context of a combination of the DDA method, IGOM, and edge effect contributions. Figure 4(b) is similar to Fig. 4(a), except that the aspect ratios for Fig. 4(b) are $0.30\!:\!0.70\!:\!1.0$. Again, a smooth transition from the DDA solutions to the IGOM results is noticed.

Figure 5 shows the integrated single-scattering properties at $12.0\,\mu$m wavelength for two aspect ratios. The refractive index at this wavelength is $1.5502 + i0.0916$, which means that ellipsoids are quite absorptive. Similar to the cases shown in Fig. 4, the results from the DDA converge to those from the IGOM but more smoothly. The results from the IGOM are more accurate in those cases having stronger absorption.

Note that we did not consider the edge effect contribution in the asymmetry factor computation, but the asymmetry factor calculated from the DDA also converges to that from the IGOM. This is due to the fact that diffraction dominates the scattered
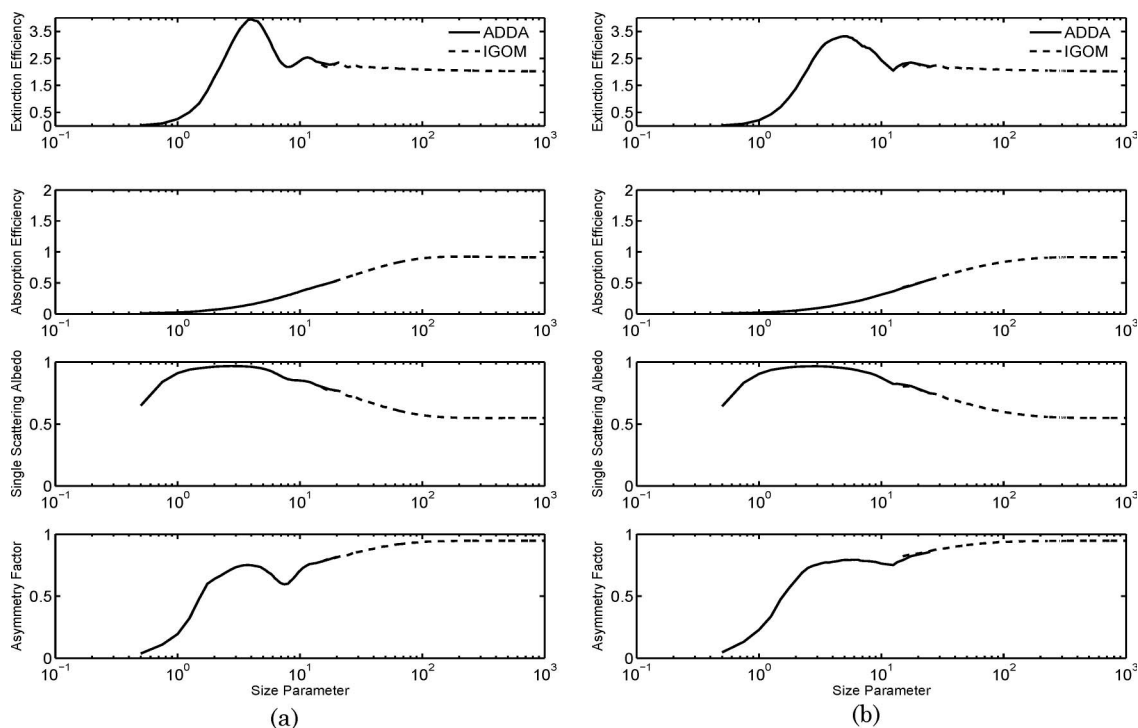

Fig. 4. Integrated single-scattering properties (extinction efficiency, absorption efficiency, single-scattering albedo, and asymmetry factor) of randomly oriented ellipsoids. The wavelength is $0.66\,\mu$m, the complex refractive index is $1.53 + 0.008i$, and the aspect ratios are $a\!:\!b\!:\!c = 0.53\!:\!0.71\!:\!1.00$ and $a\!:\!b\!:\!c = 0.30\!:\!0.70\!:\!1.00$ for left and right panels, respectively.
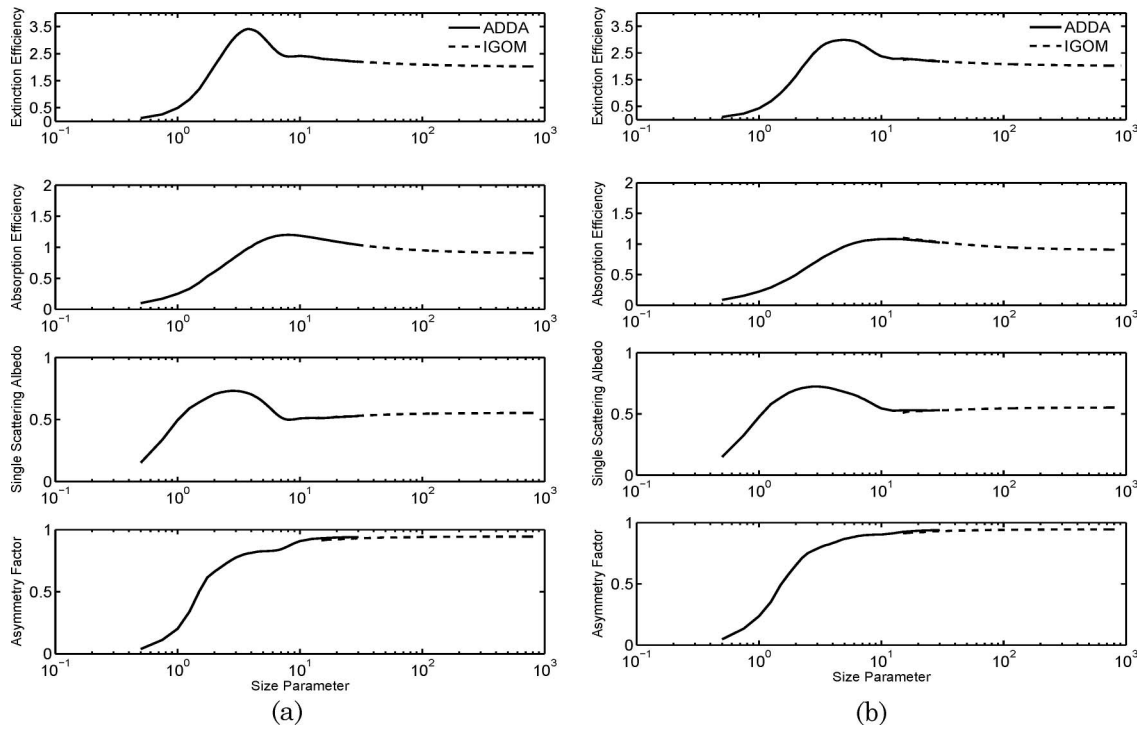
Fig. 5. Same as Fig. 4 except that the wavelength is $12\,\mu m$. The complex refractive index is $1.5502 + 0.0916i$. The aspect ratios are (a) $a\!:\!b\!:\!c = 0.53\!:\!0.71\!:\!1.00$ and (b) $a\!:\!b\!:\!c = 0.30\!:\!0.70\!:\!1.00$.

intensity pattern. The edge effect correction to the phase function should slightly influence the asymmetry factor.

B. Phase Matrix

In this section we compare the nonzero phase matrix elements computed by the DDA method and the IGOM. We consider two wavelengths corresponding to weak and strong absorption and two axis ratios $(0.53\!:\!0.71\!:\!1$ and $0.30\!:\!0.70\!:\!1.0)$. The size parameter is defined in terms of a volume-equivalent sphere and is assumed to be 30 for all the cases.

In Fig. 6, the wavelength we considered is $0.66\,\mu m$, and the axis ratios are $0.53\!:\!0.71\!:\!1$ and $0.30\!:\!0.70\!:\!1.0$ for the left and right panels, respectively. The excellent agreement between the phase functions (P_{11}) from the two methods is found. For other phase matrix elements, differences are noticeable. Figures 6(a) and 6(b) are quite different for each nonzero element. This means that the phase matrix elements are sensitive to the axis ratios of ellipsoids. For the P_{11} element, the phase function in (b) is quite featureless, whereas the phase function in (a) has some features.

Figure 7 shows nonzero phase matrix elements at $12\,\mu m$ wavelength. The axis ratios are also assumed to be $0.53\!:\!0.71\!:\!1$ and $0.30\!:\!0.70\!:\!1.0$ for the left and right panels, respectively. In Fig. 7, the agreement of the phase function (P_{11}) from the two methods is also observed. The differences for other elements are still noticeable; however, the IGOM results turn out to be better for the case with strong absorption. The fact that the accuracy of the IGOM is related to the ab-

sorption has also been reported in a previous study [11]. The curves for P_{12} from the DDA method and IGOM agree with each other when θ is larger than 90°. In comparison with weak absorption cases, the phase matrix elements for $12\,\mu m$ are quite smooth without pronounced oscillations. Unlike Fig. 6, Figs. 7(a) and 7(b) are quite similar. The reason is that, in the strong absorption case, external reflection and diffraction dominate the scattering process, and internal reflection and refraction are quite weak. Therefore, the single-scattering quantities are not sensitive to the axis ratios, especially, under random orientation conditions.

C. Comparison Between Simulation and Measurement

To examine the applicability of an ellipsoidal model to realistic dust particle bulk scattering property simulation, we compare the simulated phase function with that from laboratory measurement for feldspar aerosol particles. The full scattering phase matrix was measured by Volten *et al.* [5] at wavelengths 0.442 and $0.633\,\mu m$. We choose the $0.633\,\mu m$ case for the comparison of the simulations of the phase matrix elements against their experimental counterparts. The measured data of the bulk phase matrix elements are for a scattering angle 5°–173°, and the phase function (i.e., P_{11}) is normalized to 1 at 30°. Measurements near forward and backward scattering were not carried out due to technical difficulties. The size distributions of feldspar samples were provided by Volten *et al.* [5] along with the effective radii. The effective variance was assumed to be 1.0. Nousiainen and Vermeulen [52] employed a
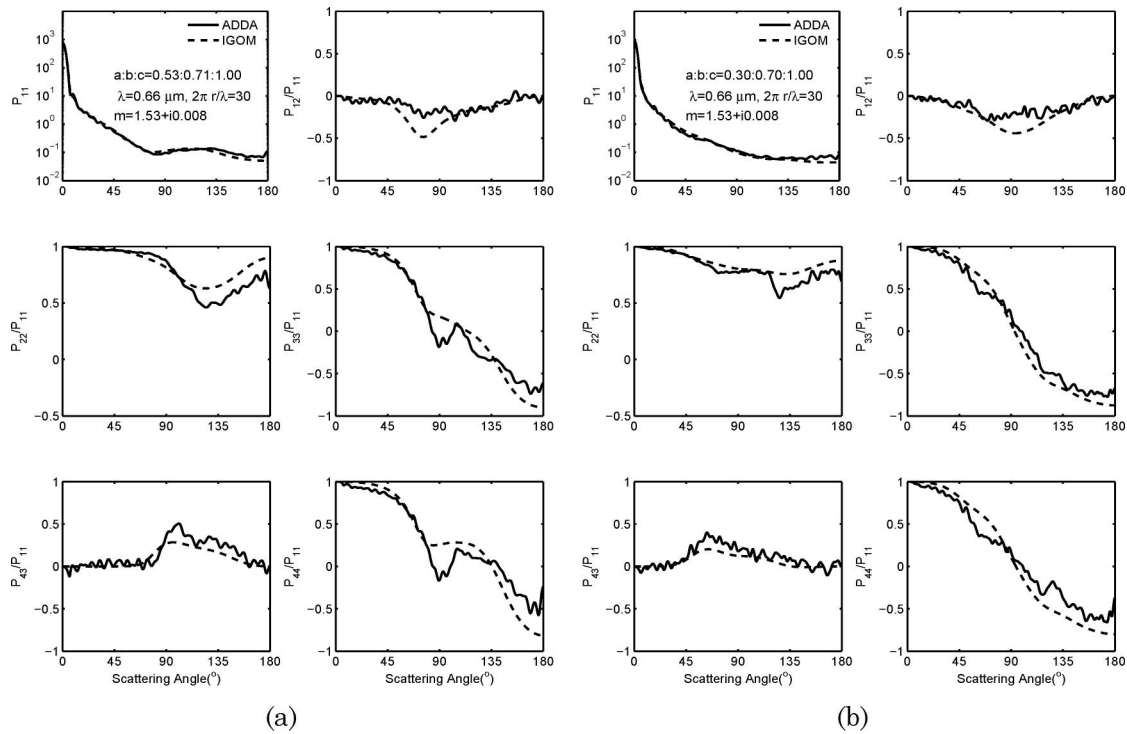
Fig. 6. Comparison of the phase matrix of an ellipsoid computed from the IGOM and DDA method at a size parameter of 30. The aspect ratios are (a) $0.53\!:\!0.71\!:\!1.0$ and (b) $0.30\!:\!0.70\!:\!1.0$.

lognormal size distribution:

$$n(r) = \frac{N_{\text{tot}}}{\sqrt{2\pi}\ln(10)\log(\sigma)r}\exp\left\{-\frac{[\log(r)-\log(R)]^2}{2[\log(\sigma)]^2}\right\},$$

(38)

where R is the mean radius and σ is the geometric standard deviation, which is specified by fitting the formula to the measured size distribution. With $R = 0.167\,\mu$m and $\sigma = 2.32$ in Eq. (38), the effective radius and variance for the fitted size distribution
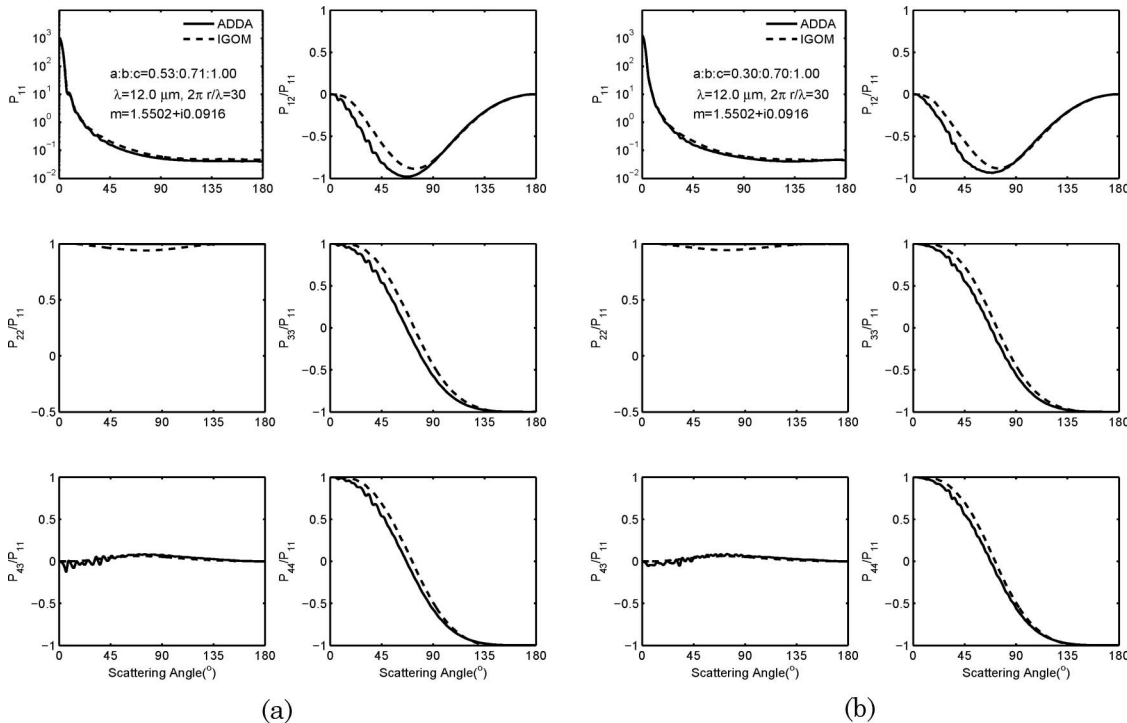

Fig. 7. Same as Fig. 6 except the wavelength is $12\,\mu$m. The aspect ratios are (a) $0.53\!:\!0.71\!:\!1.0$ and (b) $0.30\!:\!0.70\!:\!1.0$.

are $0.98\,\mu\text{m}$ and 1.02, respectively, when $r \in [0.08, 100]\,\mu\text{m}$.

The measured phase matrix of feldspar particles was compared with a theoretical simulation based on spheroidal shapes [52]. It demonstrates that using spheroids was far superior to using spheres for approximating nonspherical feldspar particle shapes in scattering computation. Ellipsoids have one more degree of freedom and lower symmetry than spheroids. Thus, it is expected that ellipsoids offer a better approximation of realistic irregular particles. To test this speculation, we first compute the bulk scattering properties of spheroids from a combination of the T-matrix simulations [19] and the present IGOM for the lognormal size distribution in Eq. (38). To match the experimental data, four sets of aspect ratios $(0.4583:1, 0.6481:1, 0.5477:1, \text{and } 0.4472:1)$ are assumed for spheroids in the bulk scattering phase matrix computation via the following formula:

$$\langle P_{ij} \rangle = \frac{\sum_{k=1}^{4} W_k \int P_{ij}^k(r) \sigma_{\text{sca}}^k(r) n(r) \text{d}r}{\sum_{k=1}^{4} W_k \int \sigma_{\text{sca}}^k(r) n(r) \text{d}r}, \qquad (39)$$

where P_{ij}^k is the normalized P_{ij} element for the kth axis ratio, σ^k is the corresponding scattering cross section, and W_k is the corresponding weight. The best agreement between the theoretical and experimental results is achieved when the weights for the four aspect ratios are 0.4444, 0.0525, 0.1676, and 0.3357.

Furthermore, we define volume-equivalent ellipsoids, and define the c axis of an ellipsoid to be the same as that of its volume-equivalent spheroid. However, the lengths of the other two axes of the ellipsoid are different, so a triaxial ellipsoid is formed. We select four sets of aspect ratios, which are given by $a:b:c = 0.3:0.7:1$, $0.6:0.7:1$, $0.5:0.6:1$, and $0.4:0.5:1$. The best agreement between the measurements and theoretical simulations is observed when the weights are selected as 0.3168, 0.0683,
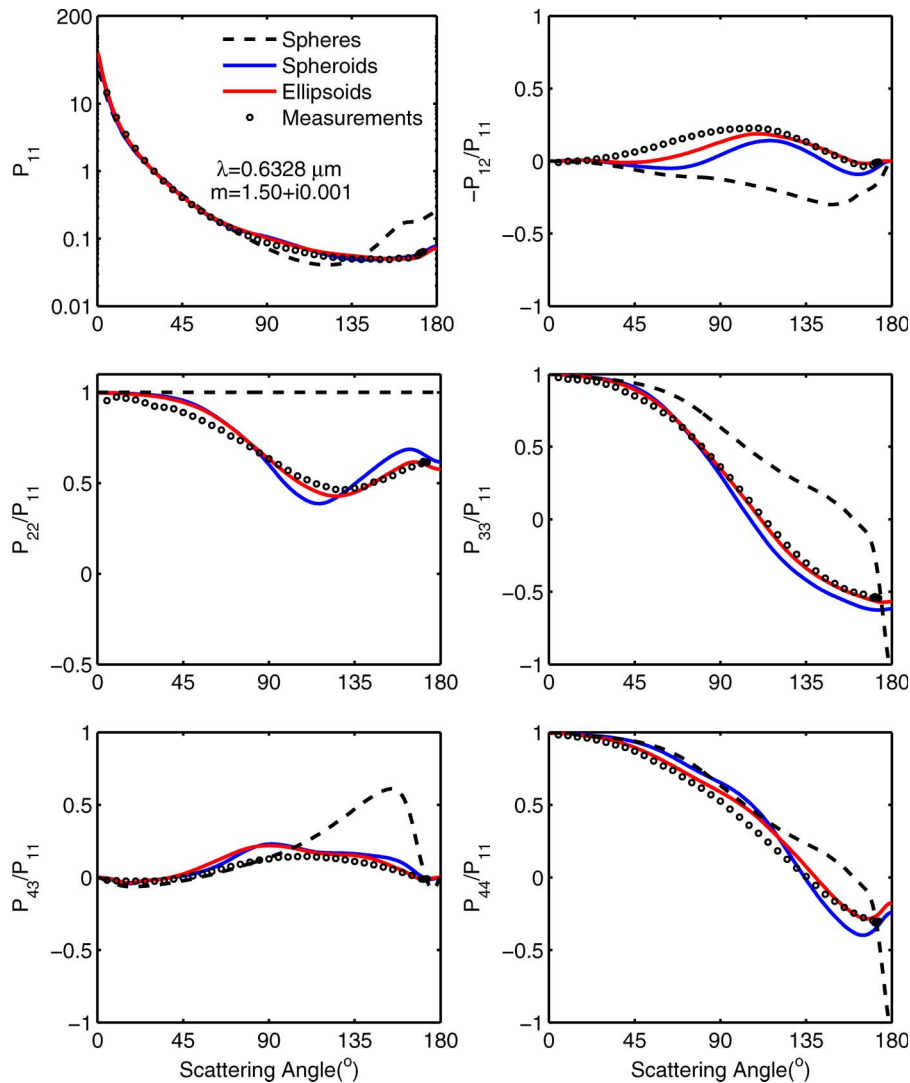

Fig. 8. (Color online) Comparison of the bulk phase function from laboratory measurement [5] with the present simulations based on spherical, spheroidal, and ellipsoidal models.

0.1730, and 0.4420 for aspect ratios $a:b:c = 0.3:0.7:1$, $0.6:0.7:1$, $0.5:0.6:1$, and $0.4:0.5:1$, respectively. Figure 8 shows the comparison between the measured phase matrix and the theoretical simulations based on spherical, spheroidal, and ellipsoidal shapes. The simulated P_{11} values are normalized to 1 at scattering angle $\theta_s = 30°$. It is evident that the phase matrix elements simulated on the basis of the ellipsoid model (red lines) agree better with the measured data than those based on the spheroid model (blue lines), whereas the sphere model (dashed black lines) leads to much larger discrepancies, particularly, in backward directions ($>90°$). The phase functions (P_{11}) simulated from the spheroid and ellipsoid models are quite similar. However, in terms of agreement with the measurements, the ellipsoid model is more accurate than the spheroid model for simulating the other phase matrix elements associated with polarization, particularly, in the cases of $-P_{12}/P_{11}$, P_{22}/P_{11}, P_{33}/P_{11}, and P_{44}/P_{11} for scattering angles larger than $90°$.

Note that we used only four aspect ratios for spheroids and ellipsoids. This case study demonstrates that the ellipsoid model is better than the spheroid model for simulating the polarization characteristics of nonspherical feldspar particles. Selecting an optimized shape (i.e., aspect ratio) distribution of ellipsoids in the optical property computation for realistic dust particles deserves further investigation.

6. Conclusions

We studied the scattering properties of randomly oriented triaxial ellipsoids with size parameters from the Rayleigh to geometric-optics regimes. The DDA is applied to compute small particle scattering properties. For moderate and large particles, we employ the IGOM, which is an approximate method based on the ray-tracing technique. To the best of our knowledge, it is the first time that the edge effect contributions to both the extinction and absorption efficiencies for ellipsoids have been studied. The present results show that the integrated scattering properties, such as the extinction efficiency, absorption efficiency, and asymmetry factor, from the DDA method smoothly transition to those simulated from the IGOM when the size parameter increases from the Rayleigh regime to the geometric-optics regime. The phase matrix elements from both methods resemble each other when size parameters are larger than 30. Therefore, a complete set of ellipsoidal particle optical properties can be efficiently calculated by combining the DDA method and the IGOM, although the phase matrix from the IGOM for moderate size particles is still in need of improvement. It should be pointed out that we can also employ the FDTD, PSTD, and T-matrix methods for small particles.

In previous studies, spheroid geometry is usually used as a simple geometry to model the scattering and radiative properties of rounded aerosol particles. The advantage of ellipsoid geometry is its lower de-

gree of symmetry. In this study, the applicability of ellipsoidal shape approximations has been validated by comparison with theoretical and experimental results for the bulk scattering matrix associated with feldspar aerosol particles. It is shown that the ellipsoid model is better than the spheroid model for simulating dust particle optical properties, particularly, their polarization characteristics, realistically. Since the single-scattering properties of ellipsoids can be efficiently computed, the ellipsoidal shape, as a simplified theoretical model for nonspherical particles, can be useful for modeling the scattering properties of irregular dustlike particles in the atmosphere.

Appendix A: Radius of Curvature in Eq. (22)

The equation of the curve of the particle boundary can be expressed in the incident coordinate system in terms of the parameter $\chi(0\,2\pi)$ as follows:

$$x'(\chi) = \bar{a}\cos\omega\cos\chi + \bar{b}\sin\omega\sin\chi, \quad (A1)$$

$$y'(\chi) = -\bar{a}\sin\omega\cos\chi + \bar{b}\cos\omega\sin\chi, \quad (A2)$$

$$z'(\chi) = -E(\chi)/D. \quad (A3)$$

Since the arc length ds is a scalar that should be the same in different Cartesian coordinate systems, we can write

$$ds = \sqrt{\bar{a}^2\sin^2\chi + \bar{b}^2\cos^2\chi}\,d\chi. \quad (A4)$$

At each point p on the edge, the "profile" defined by van de Hulst [35] is a curve through p that has its local tangent vector along the incident direction. With the common tangent vector of the "profile", there are many curves on the ellipsoidal surface whose radii of curvature are different but have the same normal radius. Consider another incident light that propagates along the tangent vector of the edge (different from the tangent vector along the incident direction). In this case, we can define an imaginary boundary curve similar to that described in Subsection 3.A. The radius of normal curvature of the imaginary boundary can be calculated, which is the same as the radius of curvature of the "profile". For convenience, let the new imaginary incident coordinate system be $o\tilde{x}\tilde{y}\tilde{z}$. The equation of the imaginary curve can be parameterized with respect to its $\tilde{y}$ component as follows:

$$\vec{r}(\tilde{y}) = [\tilde{x}(\tilde{y}), \tilde{y}, \tilde{z}(\tilde{y})]. \quad (A5)$$

According to the theory of differential geometry, the radius of curvature at the point P is given by

$$R_1 = \left|\frac{\mathrm{d}\vec{r}}{\mathrm{d}\tilde{y}}\right|^{3/2} \bigg/ \left|\frac{\mathrm{d}\vec{r}}{\mathrm{d}\tilde{y}} \times \frac{\mathrm{d}^2\vec{r}}{\mathrm{d}\tilde{y}^2}\right|, \qquad (A6)$$

where the first and second derivatives are expressed as

$$\mathrm{d}\vec{r}(\tilde{y})/\mathrm{d}\tilde{y} = (\mathrm{d}\tilde{x}(\tilde{y})/\mathrm{d}\tilde{y}, 1, \mathrm{d}\tilde{z}(\tilde{y})/\mathrm{d}\tilde{y}), \qquad (A7)$$

$$\mathrm{d}^2\vec{r}(\tilde{y})/\mathrm{d}\tilde{y}^2 = (\mathrm{d}^2\tilde{x}(\tilde{y})/\mathrm{d}\tilde{y}^2, 0, \mathrm{d}^2\tilde{z}(\tilde{y})/\mathrm{d}\tilde{y}^2), \qquad (A8)$$

with

$$\mathrm{d}\tilde{x}(\tilde{y})/\mathrm{d}\tilde{y} = -[\tilde{x}\tilde{C} + 2\tilde{B}\tilde{y}]/[\tilde{y}\tilde{C} + 2\tilde{A}\tilde{x}], \qquad (A9)$$

$$\mathrm{d}\tilde{z}(\tilde{y})/\mathrm{d}\tilde{y} = [(a^2 - b^2)c^2 \sin\bar{\beta}\cos\bar{\beta}\sin\bar{\theta}\mathrm{d}\tilde{x}(\tilde{y})/\mathrm{d}\tilde{y} \qquad (A10)$$

$$+ [a^2(c^2 - b^2) + c^2(b^2 - a^2)\cos^2\bar{\beta}]\sin\bar{\theta}\cos\bar{\theta}]/\tilde{D}. \qquad (A11)$$

The relation between $\bar{A}, \bar{B}, \bar{C}, \bar{D}$ and $\bar{\theta}, \bar{\beta}$ are the same as in Section 1. To obtain the normal radius of curvature, we first define the unit curvature vector $\hat{\tau}$, which is

$$\hat{\tau} = \hat{\gamma} \times \hat{\alpha}, \qquad (A12)$$

$$\hat{\alpha} = \mathrm{d}\vec{r}(\tilde{y})/\mathrm{d}\tilde{y}/|\mathrm{d}\vec{r}(\tilde{y})/\mathrm{d}\tilde{y}|, \qquad (A13)$$

$$\hat{\gamma} = [\mathrm{d}\vec{r}(\tilde{y})/\mathrm{d}\tilde{y} \times \mathrm{d}^2\vec{r}(\tilde{y})/\mathrm{d}\tilde{y}^2]/|\mathrm{d}\vec{r}(\tilde{y})/\mathrm{d}\tilde{y} \times \mathrm{d}^2\vec{r}(\tilde{y})/\mathrm{d}\tilde{y}^2|. \qquad (A14)$$

Finally, according to Meusnier's theorem, the radius of normal curvature is

$$R = R_1/|\hat{\tau} \cdot \hat{n}|, \qquad (A15)$$

where $\hat{n}$ is the normal direction vector at the tangent point P. Once we know R, Q_{edge} can be calculated by using a numerical integration technique (e.g., Gaussian quadrature).

References

1. M. I. Mishchenko, A. A. Lacis, B. E. Carlson, and L. D. Travis, "Nonsphericity of dust-like tropospheric aerosols: implications for aerosol remote sensing and climate modeling," Geophys. Res. Lett. **22**, 1077–1080 (1995).
2. Y. Liu, W. P. Arnott, and J. Hallertt, "Particle size distribution retrieval from multispectral optical depth: influences of particle nonsphericity and refractive index," J. Geophys. Res. **104**, 31753–31762 (1999).
3. R. Kahn, R. West, D. McDonald, B. Rheingans, and M. I. Mishchenko, "Sensitivity of multiangle remote sensing observations to aerosol sphericity," J. Geophys. Res. **102**, 16861–16870 (1997).
4. O. V. Kalashnikova and I. N. Sokolik, "Importance of shapes and compositions of wind-blown dust particles for remote sensing at solar wavelengths," Geophys. Res. Lett. **29**, doi:10.1029/2002GL014947 (2002).
5. H. Volten, O. Muñoz, E. Rol, J. F. de Haan, W. Vassen, J. W. Hovenier, K. Muinonen, and T. Nousiainen, "Scattering matrices of mineral particles at 441.6 nm and 632.8 nm," J. Geophys. Res. **106**, 17375–17401 (2001).
6. A. Macke and M. I. Mishchenko, "Applicability of regular particle shapes in light scattering calculations for atmospheric ice particles," Appl. Opt. **35**, 4291–4296 (1996).
7. F. M. Kahnert, J. J. Stamnes, and K. Stamnes, "Can simple particle shapes be used to model scalar optical properties of an ensemble of wavelength-sized particles with complex shapes?," J. Opt. Soc. Am. A **19**, 521–531 (2002).
8. M. I. Mishchenko, L. D. Travis, R. A. Kahn, and R. A. West, "Modeling phase functions for dustlike tropospheric aerosols using a shape mixture of randomly oriented polydisperse spheroids," J. Geophys. Res. **102**, 831-16–847 (1997).
9. O. Dubovik, B. N. Holben, T. Lapyonok, A. Sinyuk, M. I. Mishchenko, P. Yang, and I. Slutsker, "Non-spherical aerosol retrieval method employing light scattering by spheroids," Geophys. Res. Lett. **29**, doi:10.1029/2001GL014506 (2002).
10. O. Dubovik, A. Sinyuk, T. Lapyonok, B. N. Holben, M. I. Mishchenko, P. Yang, T. F. Eck, H. Volten, O. Munoz, B. Veihelmann, W. J. van der Zande, J. F. Leon, M. Sorokin, and I. Slutsker, "Application of spheroid models to account for aerosol particle nonsphericity in remote sensing of desert dust," J. Geophys. Res. **111**, doi:10.1029/2005JD006619 (2006).
11. P. Yang, Q. Feng, G. Hong, G. W. Kattawar, W. J. Wiscombe, M. I. Mishchenko, O. Dubovik, I. Laszlo, and I. N. Sokolik, "Modeling of the scattering and radiative properties of nonspherical dust particles," J. Aerosol. Sci. **38**, 995–1014 (2007).
12. P. Yang, K. N. Liou, M. I. Mishchenko, and B.-C. Gao, "Efficient finite-difference time domain scheme for light scattering by dielectric particles: application to aerosols," Appl. Opt. **39**, 3727–3737 (2000).
13. O. V. Kalashnikova, R. Kahn, I. N. Sokolik, and W.-H. Li, "Ability of multiangle remote sensing observations to identify and distiguish mineral dust types: optical models and

retrievals of optically thick plumes," J. Geophys. Res. **110**, D18S14, doi:10.1029/2004JD004550 (2005).

14. B. Veihelmann, "Sunlight on atmospheric water vapor and mineral aerosol : modeling the link between laboratory data and remote sensing," Ph.D. thesis (Radboud University Nijmegen, 2005).

15. S. I. Ghobrial and S. M. Sharief, "Microwave attenuation and cross polarization in dust storms," IEEE. Trans. Antennas. Propagat. **35**, 418–425 (1987).

16. F. Möglich, "Beugungerscheinungen an körpern von ellipsoidischer gestalt," Ann. Phys. **83**, 609 (1927).

17. B. D. Sleeman, "The scalar scattering of a plane wave by an ellipsoid," J. Instr. Math. Appl. **3**, 4–15 (1967).

18. A. F. Stevenson, "Solution of electromagnetic scattering problems as power series in the ratio (dimension of scatterer) wavelength," J. Appl. Phys. **24**, 1134–1142 (1953).

19. M. I. Mishchenko and L. D. Travis, "Light scattering by polydispersions of randomly oriented spheroids with sizes comparable to wavelengths of observations," Appl. Opt. **33**, 7206–7225 (1994).

20. T. Wriedt, "Using the *T*-matrix method for light scattering computations by non-axisymmetric particles: superellipsoids and realistically shaped particles," Part. Part. Syst. Charact. **19**, 256–268 (2002).

21. J. B. Schneider and I. C. Peden, "Differential cross section of a dielectric ellipsoid by the *T*-matrix extended boundary condition method," IEEE Trans. Antennas Propag. **36**, 1317–1321 (1988).

22. G. T. Draine and P. J. Flatau, "User Guide to the Discrete Dipole Approximation Code DDSCAT6.1," http://arxiv.org/abs/astro-ph/0409262v2 (2004).

23. M. A. Yurkin and A. G. Hoekstra, "Amsterdam DDA," http://www.science.uva.nl/research/scs/oftware/adda (2007).

24. A. Taflove and S. C. Hagness, *Advances in Computational Electrodynamics: the Finite-Difference-Time-Domain Method*, 3rd ed. (Artech House, 2005).

25. P. Yang and K. N. Liou, "Finite difference time domain method for light scattering by nonspherical and inhomogeneous particles," in *Light Scattering by Nonspherical Particles, Theory, Measurements, and Applications*, M. I. Mishchenko, J. W. Hovenier, and L. D. Travis, eds. (Academic, 2000), pp. 173–221.

26. Q. H. Liu, "The pseudospectral time-domain (PSTD) algorithm for acoustic waves in absorptive media," IEEE Trans. Ultrason. Ferroelectr. Freq. Control **45**, 1044–1055 (1998).

27. G. Chen, P. Yang, and G. W. Kattawar, "Application of the pseudospectral time-domain method to the scattering of light by nonspherical particles," J. Opt. Soc. Am. A **25**, 785–790 (2008).

28. G. J. Streekstra, A. G. Hoekstra, and R. M. Heethaar, "Anomalous diffraction by arbitrarily oriented ellipsoids: applications in ektacytometry," Appl. Opt. **33**, 7288–7296 (1994).

29. P. Mazeron and S. Muller, "Light scattering by ellipsoids in a physical optics approximation," Appl. Opt. **35**, 3726–3735 (1996).

30. P. Yang and K. N. Liou, "Geometric-optics-integral-equation method for light scattering by nonspherical ice crystals," Appl. Opt. **35**, 6568–6584 (1996).

31. D. S. Jones, "Approximate methods in high-frequency scattering," Proc. R. Soc. A **239**, 338–348 (1957).

32. D. S. Jones, "High-frequency scattering of electromagnetic waves," Proc. R. Soc. Lond. A **240**, 206–213 (1957).

33. G. R. Fournier and B. T. N. Evans, "Approximation to extinction efficiency for randomly oriented spheroids," Appl. Opt. **30**, 2042–2048 (1991).

34. J. Zhao and Y. Hu, "Bridging technique for calculating the extinction efficiency of arbitrary shaped particles," Appl. Opt. **42**, 4931–4945 (2003).

35. H. C. van de Hulst, *Light Scattering by Small Particles* (Wiley, 1957).

36. A. J. Baran and S. Havemann, "Rapid computation of the optical properties of hexagonal columns using complex angular momentum theory," J. Quant. Spectrosc. Radiat. Transfer **63**, 499–519 (1999).

37. D. L. Mitchell, W. P. Arnott, C. Schmitt, A. J. Baran, S. Havemann, and Q. Fu, "Contributions of photon tunneling to extinction in laboratory grown hexagonal columns," J. Quant. Spectrosc. Radiat. Transfer **70**, 761–776 (2001).

38. D. L. Mitchell, A. J. Baran, W. P. Arnott, and C. Schmitt, "Testing and comparing the modified anomalous diffraction approximation," J. Atmos. Sci. **63**, 2948–2962 (2006).

39. H. M. Nussenzveig and W. J. Wiscombe, "Efficiency factors in Mie scattering," Phys. Rev. Lett. **45**, 1490–1494 (1980).

40. H. M. Nussenzveig and W. J. Wiscombe, "Complex angular momentum approximation to hard-core scattering," Phys. Rev. A **43**, 2093–2112 (1991).

41. H. M. Nussenzveig, *Diffraction Effects in Semiclassical Scattering* (Cambridge University, 1992).

42. F. M. Kahnert, "Numerical methods in electromagnetic scattering theory," J. Quant. Spectrosc. Radiat. Transfer **79**, 775–824 (2003).

43. E. M. Purcell and C. R. Pennypacker, "Scattering and absorption of light by nonspherical dielectric grains," Astrophys. J. **186**, 705–714 (1973).

44. B. T. Draine, "The discrete-dipole approximation and its application to interstellar graphite grains," Astrophys. J. **333**, 848–872 (1988).

45. G. H. Goedecke and S. G. O'Brien, "Scattering by irregular inhomogeneous particles via the digitized Green's function algorithm," Appl. Opt. **27**, 2431–2438 (1988).

46. M. A. Yurkin and A. G. Hoekstra, "The discrete dipole approximation: an overview and recent developments," J. Quant. Spectrosc. Radiat. Transfer **106**, 558–589 (2007).

47. G. Hong, P. Yang, F. Z. Weng, and Q. H. Liu, "Microwave scattering properties of sand particles: application to the simulation of microwave radiances over sandstorms," J. Quant. Spectrosc. Radiat. Transfer. **109**, 684–702 (2008).

48. P. Wendling, R. Wendling, and H. K. Weickmann, "Scattering of solar radiation by hexagonal ice crystals," Appl. Opt. **18**, 2663–2671 (1979).

49. S. I. Rubinow and T. T. Wu, "First correction to the geometric-optics scattering cross section from cylinders and spheres," J. Appl. Phys. **27**, 1032–1039 (1956).

50. M. Abramowitz and I. A. Stegun, *Handbook of Mathematical Functions* (Dover, 1972).

51. C. Levoni, M. Cervino, R. Guzzi, and F. Torricella, "Atmospheric aerosol optical properties: a database of radiative characteristics for different components and classes," Appl. Opt. **36**, 8031–8041 (1997).

52. T. Nousiainen and K. Vermeulen, "Comparison of measured single-scattering matrix of feldspar particles with *T*-matrix simulations using spheroids," J. Quant. Spectrosc. Radiat. Transfer **79**, 1031–1042 (2003).